

# Simulating Seismic Wave Propagation in 3D Elastic Media Using Staggered-Grid Finite Differences

by Robert W. Graves

**Abstract** This article provides an overview of the application of the staggered-grid finite-difference technique to model wave propagation problems in 3D elastic media. In addition to presenting generalized, discrete representations of the differential equations of motion using the staggered-grid approach, we also provide detailed formulations that describe the incorporation of moment-tensor sources, the implementation of a stable and accurate representation of a planar free-surface boundary for 3D models, and the derivation and implementation of an approximate technique to model spatially variable anelastic attenuation within time-domain finite-difference computations. The comparison of results obtained using the staggered-grid technique with those obtained using a frequency-wavenumber algorithm shows excellent agreement between the two methods for a variety of models. In addition, this article also introduces a memory optimization procedure that allows large-scale 3D finite-difference problems to be computed on a conventional, single-processor desktop workstation. With this technique, model storage is accommodated using both external (hard-disk) and internal (core) memory. To reduce system overhead, a cascaded time update procedure is utilized to maximize the number of computations performed between I/O operations. This formulation greatly expands the applicability of the 3D finite-difference technique by providing an efficient and practical algorithm for implementation on commonly available workstation platforms.

## Introduction

Modern computational efficiency has advanced to a state where we can begin to calculate wave-field simulations for realistic 3D models at frequencies of interest to both seismologists and engineers. The most general of these numerical methods are grid-based techniques that track the wave field on a dense 3D grid of points, e.g., the finite-difference (FD), finite-element (FE), and pseudospectral (PS) methods. Various algorithms have been developed to implement these techniques, and while there will always be debate as to which one is the “best” technique, each method has its merits and pitfalls.

Our approach uses a staggered-grid finite-difference algorithm to model the first-order elastodynamic equations of motion expressed in terms of velocity and stress. In seismic applications, the velocity-stress formulation was first used by Madariaga (1976) to model fault-rupture dynamics. Virieux (1984, 1986) and Levander (1988) have since extended the technique to model seismic wave propagation in 2D media, and the formulation for 3D media is outlined by Randall (1989) and Yomogida and Etgen (1993). The advantages of the staggered-grid formulation are (1) source insertion is straightforward and can be expressed in terms of velocity (via body forces) or stress; (2) a stable and accurate repre-

sentation for a planar free-surface boundary is easily implemented; (3) since the finite-difference operators are local, the entire model does not have to reside in core memory all at once; (4) it is easily extended to high-order spatial difference operators; (5) the method can be interfaced with other modeling techniques by expressing the input wave field along a boundary of the finite-difference grid; and (6) the algorithm is easily implemented on scalar, vector, or parallel computers.

In the following sections, we outline the numerical approach beginning with the equations of motion and then describe their discrete formulation using the staggered-grid approach. We do not provide a detailed analysis of the development of absorbing boundary conditions, stability of the numerical system, or issues regarding numerical grid dispersion, as these topics are all adequately covered in the before-mentioned articles. We do, however, discuss in detail some new ideas related to incorporating earthquake (double-couple) sources, free-surface boundary implementation, and modeling spatially variable anelasticity (using  $Q$ ). In addition, we describe a memory optimization technique, which allows the computation of large-scale 3D finite-difference problems using only a single-processor desktop workstation.

The key to this memory optimization technique is a cascaded time update algorithm that maximizes the number of computations performed between successive I/O operations. Along with the presentation and discussion of these new ideas, we also show a series of comparisons between results generated by the staggered-grid finite-difference method with those generated using a frequency-wavenumber integration technique. These comparisons demonstrate the high degree of accuracy and utility of the staggered-grid technique.

### Equations of Motion

The following sets of equations describe wave propagation within three-dimensional (3D), linear, isotropic elastic media.

Equations of momentum conservation:

$$\begin{aligned}\rho\partial_t u_x &= \partial_x \tau_{xx} + \partial_y \tau_{xy} + \partial_z \tau_{xz} + f_x, \\ \rho\partial_t u_y &= \partial_x \tau_{xy} + \partial_y \tau_{yy} + \partial_z \tau_{yz} + f_y, \\ \rho\partial_t u_z &= \partial_x \tau_{xz} + \partial_y \tau_{yz} + \partial_z \tau_{zz} + f_z.\end{aligned}\quad (1)$$

Stress-strain relations:

$$\begin{aligned}\tau_{xx} &= (\lambda + 2\mu)\partial_x u_x + \lambda(\partial_y u_y + \partial_z u_z), \\ \tau_{yy} &= (\lambda + 2\mu)\partial_y u_y + \lambda(\partial_x u_x + \partial_z u_z), \\ \tau_{zz} &= (\lambda + 2\mu)\partial_z u_z + \lambda(\partial_x u_x + \partial_y u_y), \\ \tau_{xy} &= \mu(\partial_y u_x + \partial_x u_y), \\ \tau_{xz} &= \mu(\partial_z u_x + \partial_x u_z), \\ \tau_{yz} &= \mu(\partial_z u_y + \partial_y u_z).\end{aligned}\quad (2)$$

In these equations,  $(u_x, u_y, u_z)$  are the displacement components;  $(\tau_{xx}, \tau_{yy}, \tau_{zz}, \tau_{xy}, \tau_{xz}, \tau_{yz})$  are the stress components;  $(f_x, f_y, f_z)$  are the body-force components;  $\rho$  is the density;  $\lambda$  and  $\mu$  are Lamé coefficients; and the symbols  $\partial_x, \partial_y, \partial_z$ , and  $\partial_t$  are shorthand representations of the differential operators  $\partial/\partial x, \partial/\partial y, \partial/\partial z$ , and  $\partial^2/\partial t^2$ .

These equations can be formulated into a set of first-order differential equations by first differentiating equations (2) with respect to time and then substituting the velocity components  $(v_x, v_y, v_z)$  for the time-differentiated displacements  $\partial_t(u_x, u_y, u_z)$ . The resulting sets of equations are given by

$$\begin{aligned}\partial_t v_x &= b(\partial_x \tau_{xx} + \partial_y \tau_{xy} + \partial_z \tau_{xz} + f_x), \\ \partial_t v_y &= b(\partial_x \tau_{xy} + \partial_y \tau_{yy} + \partial_z \tau_{yz} + f_y), \\ \partial_t v_z &= b(\partial_x \tau_{xz} + \partial_y \tau_{yz} + \partial_z \tau_{zz} + f_z),\end{aligned}\quad (3)$$

where  $b = 1/\rho$  is the buoyancy, and

$$\begin{aligned}\partial_t \tau_{zz} &= (\lambda + 2\mu)\partial_x v_x + \lambda(\partial_y v_y + \partial_z v_z), \\ \partial_t \tau_{yy} &= (\lambda + 2\mu)\partial_y v_y + \lambda(\partial_x v_x + \partial_z v_z), \\ \partial_t \tau_{xx} &= (\lambda + 2\mu)\partial_z v_z + \lambda(\partial_x v_x + \partial_y v_y), \\ \partial_t \tau_{xy} &= \mu(\partial_y v_x + \partial_x v_y), \\ \partial_t \tau_{xz} &= \mu(\partial_z v_x + \partial_x v_z), \\ \partial_t \tau_{yz} &= \mu(\partial_z v_y + \partial_y v_z).\end{aligned}\quad (4)$$

### Finite-Difference Implementation

The system of equations (3) and (4) is easily solved using a staggered-grid finite-difference technique (e.g., Virieux, 1986; Levander, 1988; Randall, 1989). Details of this type of formulation can be found in the above articles, along with numerical accuracy and stability analyses. Figure 1 illustrates the layout of the wave-field variables and media parameters on the staggered-grid mesh. One of the attractive features of the staggered-grid approach is that the various difference operators are all naturally centered at the same point in space and time. Thus, the system is not only staggered on a spatial grid but also temporally, so that the velocities are updated independently from the stresses. This allows for a very efficient and concise implementation scheme.

The discrete form of equations (3) and (4) is given by

$$\begin{aligned}v_{xi+1/2,j,k}^{n+1/2} &= v_{xi+1/2,j,k}^{n-1/2} + [\Delta t \bar{b}_x (D_x \tau_{xx} \\ &\quad + D_y \tau_{xy} + D_z \tau_{xz} + f_x)]|_{i+1/2,j,k}^n \\ v_{yij+1/2,k}^{n+1/2} &= v_{yij+1/2,k}^{n-1/2} + [\Delta t \bar{b}_y (D_x \tau_{xy} \\ &\quad + D_y \tau_{yy} + D_z \tau_{yz} + f_y)]|_{i,j+1/2,k}^n \\ v_{zijk+1/2}^{n+1/2} &= v_{zijk+1/2}^{n-1/2} + [\Delta t \bar{b}_z (D_x \tau_{xz} + D_y \tau_{yz} \\ &\quad + D_z \tau_{zz} + f_z)]|_{i,j,k+1/2}^n\end{aligned}\quad (5)$$

for the velocities, and

$$\begin{aligned}\tau_{xxi,j,k}^{n+1} &= \tau_{xxi,j,k}^n + \Delta t [(\lambda + 2\mu)D_x v_x \\ &\quad + \lambda(D_y v_y + D_z v_z)]|_{i,j,k}^{n+1/2} \\ \tau_{yyij,k}^{n+1} &= \tau_{yyij,k}^n + \Delta t [(\lambda + 2\mu)D_y v_y \\ &\quad + \lambda(D_x v_x + D_z v_z)]|_{i,j,k}^{n+1/2} \\ \tau_{zzijk}^{n+1} &= \tau_{zzijk}^n + \Delta t [(\lambda + 2\mu)D_z v_z \\ &\quad + \lambda(D_x v_x + D_y v_y)]|_{i,j,k}^{n+1/2} \\ \tau_{xyi+1/2,j+1/2,k}^{n+1} &= \tau_{xyi+1/2,j+1/2,k}^n + \Delta t [\bar{\mu}_{xy}^H (D_y v_z \\ &\quad + D_x v_y)]|_{i+1/2,j+1/2,k}^{n+1/2} \\ \tau_{xzi+1/2,j,k+1/2}^{n+1} &= \tau_{xzi+1/2,j,k+1/2}^n + \Delta t [\bar{\mu}_{xz}^H (D_z v_x \\ &\quad + D_x v_x)]|_{i+1/2,j,k+1/2}^{n+1/2}\end{aligned}\quad (6)$$

Unit Cell for Staggered-Grid Formulation

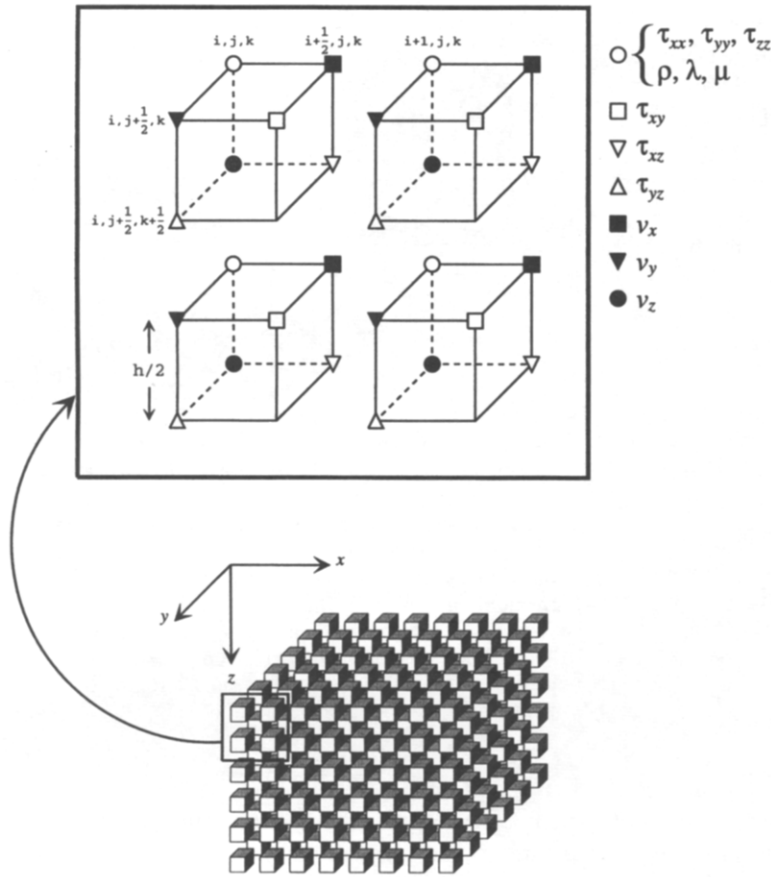


Figure 1. Grid layout for staggered-grid formulation. a unit cell consists of the wave-field variables and media parameters that are defined at a specific node, as shown in the top portion of the figure. The model space is then made up of series of repeated unit cells that occupy a 3D volume of space. The indices ( $i, j, k$ ) represent values of the spatial coordinates ( $x, y, z$ ), respectively, and the grid spacing  $h$  is defined as the length between the centers of two adjacent grid cells.

$$\tau_{yz}^{n+1/2, i, j+1/2, k+1/2} = \tau_{yz}^n{}_{i, j+1/2, k+1/2} + \Delta t [\bar{\mu}_{yz}^H (D_x v_y + D_y v_z)]^{n+1/2}{}_{i, j+1/2, k+1/2},$$

for the stresses.

In the above equations, the subscripts refer to the spatial indices, and the superscripts refer to the time index. Thus, with a grid spacing of  $h$  and a time step of  $\Delta t$ , the expression

$$v_{xi+1/2, j, k}^{n+1/2} \tag{7}$$

represents the  $x$  component of velocity evaluated at the point  $x = [i + (1/2)]h$ ,  $y = jh$ ,  $z = kh$ , and at time  $t = [n + (1/2)]\Delta t$  (see Fig. 1). We have used a second-order approximation for the time derivatives in these expressions, and the symbols  $D_x$ ,  $D_y$ , and  $D_z$  represent the discrete forms of the spatial differential operators  $\partial_x$ ,  $\partial_y$ , and  $\partial_z$ . Second- and fourth-order expressions for these discrete operators are given in Appendix A. Here, we have also introduced the effective media parameters given by

$$\begin{aligned} \bar{b}_x &= \frac{1}{2} [b_{i, j, k} + b_{i+1, j, k}] \\ \bar{b}_y &= \frac{1}{2} [b_{i, j, k} + b_{i, j+1, k}] \\ \bar{b}_z &= \frac{1}{2} [b_{i, j, k} + b_{i, j, k+1}] \end{aligned} \tag{8}$$

for the buoyancy, and

$$\begin{aligned} \bar{\mu}_{xy}^H &= \left[ \frac{1}{4} (1/\mu_{i, j, k} + 1/\mu_{i+1, j, k} + 1/\mu_{i, j+1, k} + 1/\mu_{i+1, j+1, k}) \right]^{-1} \\ \bar{\mu}_{xz}^H &= \left[ \frac{1}{4} (1/\mu_{i, j, k} + 1/\mu_{i+1, j, k} + 1/\mu_{i, j, k+1} + 1/\mu_{i+1, j, k+1}) \right]^{-1} \\ \bar{\mu}_{yz}^H &= \left[ \frac{1}{4} (1/\mu_{i, j, k} + 1/\mu_{i, j+1, k} + 1/\mu_{i, j, k+1} + 1/\mu_{i, j+1, k+1}) \right]^{-1} \end{aligned} \tag{9}$$

for the rigidity.

The use of effective media parameters for the staggered-grid formulation follows from the work of Randall *et al.* (1991), who applied this technique to systems with second-order spatial operators. For non-staggered-grid systems, sev-

eral investigators have employed effective media parameters in their calculations (e.g., Boore, 1972; Kummer *et al.*, 1987; Moczo, 1989; Zahradnik *et al.*, 1993). As shown by Zahradnik *et al.* (1993), the effective media parameters provide a more accurate representation of the actual parameters in the region near media interfaces by appropriately satisfying the traction continuity condition across the interface. Our numerical experiments for the fourth-order staggered-grid system show that the use of effective media parameters yields very accurate results. Furthermore, we have found that media averaging is necessary to ensure numerical stability when an interface with a large media contrast (e.g., factor of 4 or 5) intersects the free surface.

Two important points should be noted regarding the numerical implementation of equations (5) and (6). First, the differential operators only act on the wave-field variables, not on the media parameters, thus differencing of the media coefficients is not necessary in this scheme, and the complexity of the media has no impact on the form of the differential terms. Second, the time updates are computed such that the velocity field at time  $[n + (1/2)]\Delta t$  is determined explicitly from equations (5) using the velocity field at time  $[n - (1/2)]\Delta t$  and the stress field (and, possibly, body forces) at time  $n\Delta t$ . At time  $(n + 1)\Delta t$ , the stress field is then updated explicitly with equations (6) from the stress field at time  $n\Delta t$  and the previously updated velocity field at time  $[n + (1/2)]\Delta t$ . Thus, the time update scheme is very straightforward, and source implementation (stress, velocity, equivalent body force, etc.) is explicit and is accomplished by simply adding the appropriate source components to the wave field. A more detailed discussion of source specification is presented in a later section.

### Memory Optimization Procedure

Since the difference operators used in this formulation are local operators (meaning that the spatial derivatives are calculated using only a few neighboring grid points), then only a subset of the entire model space must reside in core memory at one time (Fig. 2). Not only does this ease the restriction on model size due to core memory constraints but, perhaps more importantly, the time-stepping algorithm can then be easily formulated so as to maximize the number of time updates that are performed on the model subset for each I/O operation. We refer to this procedure as the memory optimization algorithm, and its implementation is illustrated schematically in Figures 3a and 3b.

In Figure 3a, the computation is initiated using a “roll-in” procedure to bring a subset of the model space into core memory. In this figure, the shaded boxes represent 2D planes of the model space taken at discrete locations along the  $y$  axis, which are stored in core memory. Each plane contains either the velocity or stress components of the wave field at a given time step for all  $x$  and  $z$  locations in that plane. Velocities and stresses are updated using equations (5) and (6), as shown schematically in the upper left panel of this

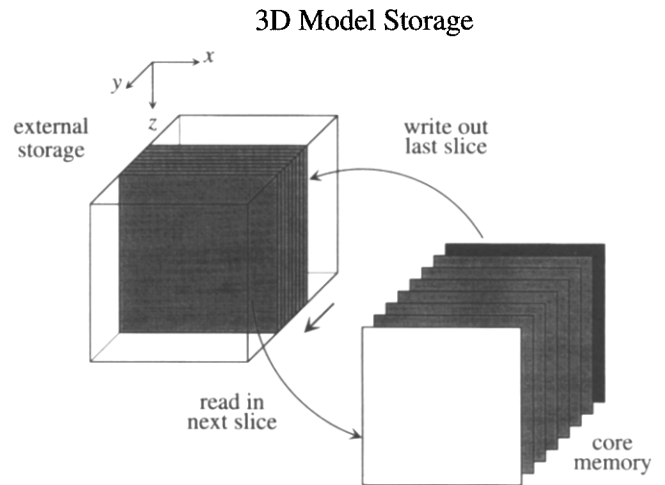


Figure 2. Schematic diagram illustrating the division of the model space between external (disk) and internal (core) memory. Because the difference operators are local, only a subset of the model space needs to reside in core memory at one time. In this scheme, individual slices of the model are pushed through core memory in a pipeline fashion as the computations proceed, eventually sweeping out the entire model space. Each slice of the model is composed of two  $xz$  planes (one for the velocity field and one for the stress field) centered at a given value of  $y$ .

figure. For the fourth-order system, four spatially adjacent planes are needed for the update. In addition, the updated variable overwrites (in memory) the value at the previous time step, as indicated by the open boxes in this figure.

To initiate the calculation, a number of velocity and stress planes are read into core memory, with the total number of stress planes being two less than the total number of velocity planes (Fig. 3a, Step 1). Next, using equations (5), velocities are updated for all possible planes ( $y_{N-4}, \dots, y_0$ ), overwriting the existing values and using an appropriate boundary condition operator at  $y_0$ . The total number of planes that can be updated will be three less than the initial number of velocity planes read into memory (Fig. 3a, Step 2). Now, using these newly updated velocity planes along with equations (6), the stress field can be updated in a similar manner. Again, the total number of updated planes is three less than the number available at the previous time step (Fig. 3a, Step 3). Steps 2 and 3 can be repeated until all possible updates have been computed for the current model subset (Fig. 3a, Step 4). It should be noted that although a number of time updates have been computed, no additional storage beyond the initial allocation is required.

Once the initial model subset has been established by the roll-in procedure described above, the remaining portion of the model can be updated using the cascaded time update scheme illustrated in Figure 3b. First, a new set of initial velocity and stress planes are read in at the next step in the  $y$  direction (Fig. 3b, Step 1). Using these new planes, a whole

series of time updates can be computed for the existing model planes that currently reside in core (Fig. 3b, Step 2). When the end of the pipeline is reached, the last set of planes is written out to hard disk (Fig. 3b, Step 3). This same sequence of steps is repeated until all planes of the model have been processed. A “roll-out” procedure similar to the roll-in procedure is then used at the end of the model. This entire process is then repeated to compute subsequent time updates.

The number of time updates that can be performed before having to read from hard disk is directly proportional to the number of planes stored in core memory. This is governed by the relation

$$NP = 4 \times NT + 2. \quad (10)$$

Here,  $NP$  is the number of planes stored in core memory, and  $NT$  is the number of time updates that can be computed before the next I/O operation. Obviously, the more core memory that is available, the greater the number of time updates that can be done between I/O operations. In typical large-scale 3D applications, 5 to 10 time updates can easily be computed for each I/O operation. This reduces I/O time to about 10 to 20% of the total CPU time and allows the method to be implemented efficiently on a workstation platform.

### Absorbing Boundary Condition

In our formulation, we use the A1 absorbing boundary condition of Clayton and Engquist (1977), as applied to the velocity components of the wave field. This is basically a normal incidence, plane wave approximation for the outgoing waves and is very easy to implement. We assume that  $P$  waves are partitioned on the velocity component perpendicular to a given model boundary and that  $S$  waves are partitioned on the velocity components oriented parallel to the model boundary. At the corners of the model 1space,  $P$ - and  $S$ -wave velocities are averaged, and this averaged wave speed is used in the application of the boundary condition for all three velocity components (i.e., no distinction is made between  $P$  and  $S$  waves at the model corners).

### Moment-Tensor Source Description

Representations of earthquake sources can be included in the staggered-grid system using either the stress components (e.g., Coutant *et al.*, 1995; Olsen *et al.*, 1995) or the velocity components (e.g., Yomogida and Etgen, 1993). Here, we present a generalized moment-tensor source formulation, which uses a distribution of body forces that are added to the individual components of velocity. Our approach basically follows the method outlined by Frankel (1993), with appropriate modifications to incorporate the staggered-grid parameterization.

The moment-tensor components can be represented as an equivalent distribution of body-force couples centered at the grid location  $x = ih$ ,  $y = jh$ ,  $z = kh$ . We will begin by

first considering the moment-tensor contributions to the  $x$  component of the body forces,  $f_x$ . These components are  $M_{xx}(t)$ ,  $M_{xy}(t)$ , and  $M_{xz}(t)$ . The  $M_{xx}(t)$  component represents a force couple having a moment arm of length  $h$  aligned in the  $x$  direction (see Fig. 4a). The strength of each force is  $M_{xx}(t)/h$ , and normalizing by the volume of the grid cell,  $h^3$ , we obtain the equivalent body-force distribution,

$$\begin{aligned} f_{x_{i+1/2,j,k}} &= \frac{M_{xx}(t)}{h^4}, \\ f_{x_{i-1/2,j,k}} &= \frac{-M_{xx}(t)}{h^4}, \end{aligned} \quad (11)$$

for this component. Similarly, we can define equivalent body-force distributions for the  $M_{xy}(t)$  and  $M_{xz}(t)$  moment-tensor components. These are given by

$$\begin{aligned} f_{x_{i-1/2,j+1,k}} &= \frac{M_{xy}(t)}{4h^4} \\ f_{x_{i+1/2,j+1,k}} &= \frac{M_{xy}(t)}{4h^4} \\ f_{x_{i-1/2,j-1,k}} &= \frac{-M_{xy}(t)}{4h^4} \\ f_{x_{i+1/2,j-1,k}} &= \frac{-M_{xy}(t)}{4h^4} \end{aligned} \quad (12)$$

for the  $M_{xy}(t)$  component, and

$$\begin{aligned} f_{x_{i-1/2,j,k+1}} &= \frac{M_{xz}(t)}{4h^4} \\ f_{x_{i+1/2,j,k+1}} &= \frac{M_{xz}(t)}{4h^4} \\ f_{x_{i-1/2,j,k-1}} &= \frac{-M_{xz}(t)}{4h^4} \\ f_{x_{i+1/2,j,k-1}} &= \frac{-M_{xz}(t)}{4h^4} \end{aligned} \quad (13)$$

for the  $M_{xz}(t)$  component. The additional factor of 4 in the normalization terms of these components arises because the length of the moment arms is  $2h$ , and two adjacent couples must be averaged in order to center the source at the proper location. These force distributions are illustrated in Figures 4b and 4c. The moment-tensor contributions to the  $y$  and  $z$  components of the body forces,  $f_y$  and  $f_z$ , can be derived in a similar fashion. These expressions are given in Appendix B.

Using equations (11) through (13) and (B1), we have a complete description of the body-force distribution required to represent the moment-tensor components. These expressions can be used to specify the source radiation for a wide range of source mechanisms (e.g., explosion, shear dislocation, etc.). In our applications, we are primarily interested in the study of earthquake sources, which can be described as shear dislocations along a planar fault. Relations between

a)

### Roll-in Model Planes

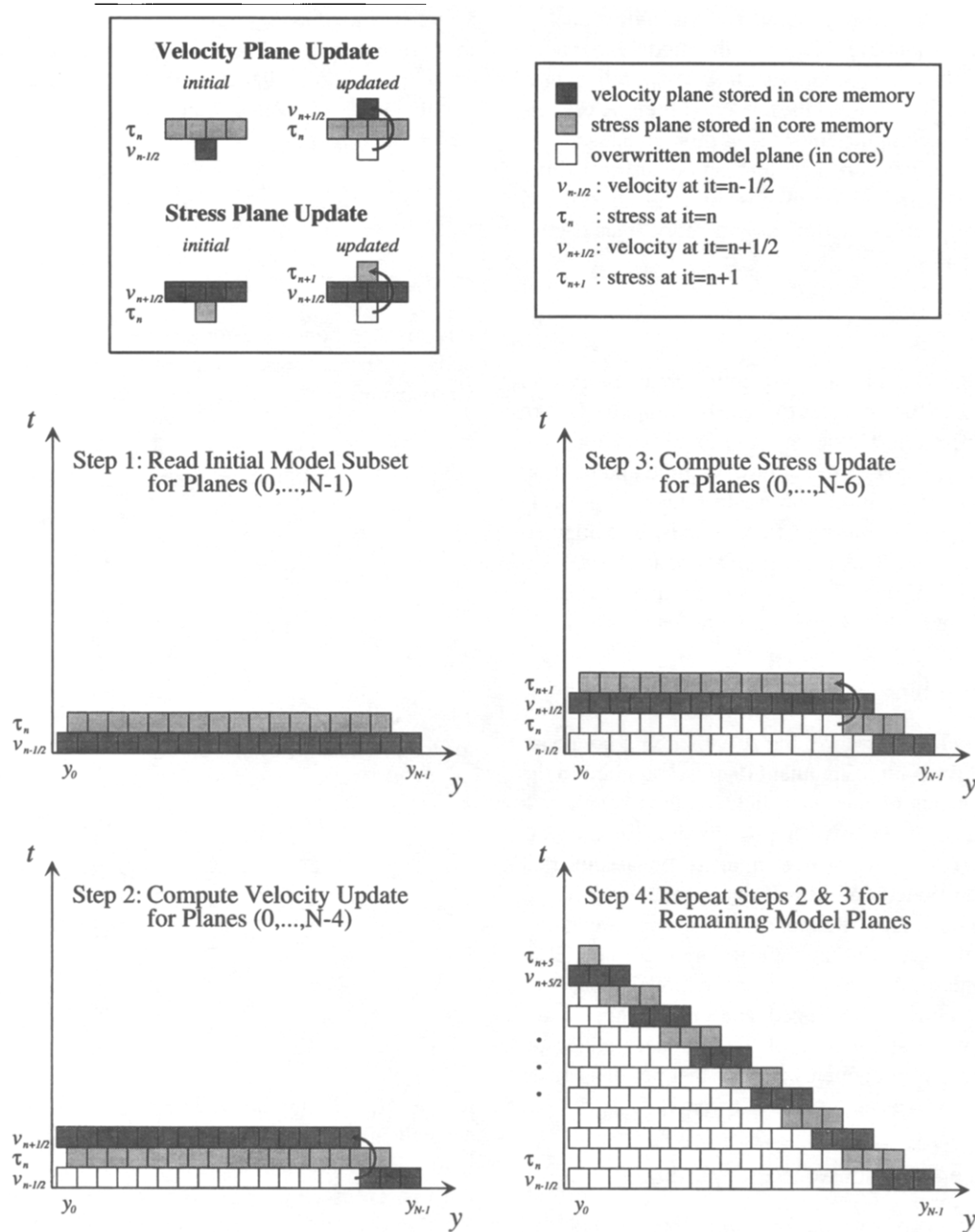


Figure 3. (a) Schematic diagram demonstrating the “roll-in” procedure to bring a subset of the model into core memory. Initially, a set of velocity and stress planes are read into core memory for  $y_0, \dots, y_{N-1}$  (step 1). Then, the velocities are updated for planes  $y_0 \dots, y_{N-4}$  (step 2). Using these updated values, the stress planes for  $y_0 \dots, y_{N-6}$  can then be updated (step 3). Steps 2 and 3 can be repeated until the remaining portion of the model subset has been updated (step 4). The model is now ready to begin the cascaded sequence of time updates illustrated in (b). (b) Schematic diagram demonstrating the optimization of the number of time update computations performed for each I/O operation from disk. For each new set of model planes read into core (step 1), a series of time updates are performed (or cascaded) through the existing model planes that currently reside in core (step 2). Finally, the last set of model planes in the pipeline is written back to disk (step 3). Typically, utilizing this type of optimization yield 5 to 10 time updates per I/O operation, significantly reducing system overhead.

b)

### Cascaded Time Update Scheme

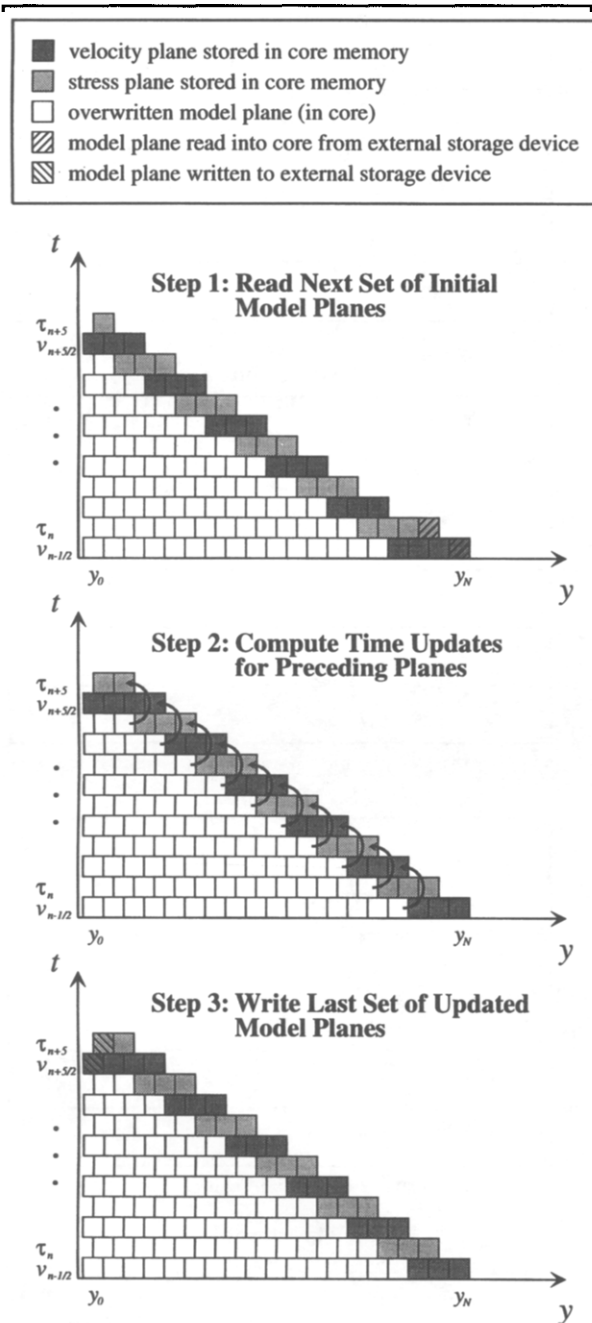


Figure 3. continued

the fault parameters strike, dip, rake, and moment, and the Cartesian components of the moment tensor are given by Aki and Richards (1980).

To demonstrate the effectiveness of this source formulation, we have performed calculations to model the seismic response for three fundamental fault orientations. These fault orientations are listed in Table 1. Following the expressions of Herrmann and Wang (1985), linear combinations of these

### Moment Tensor Components in the x-direction

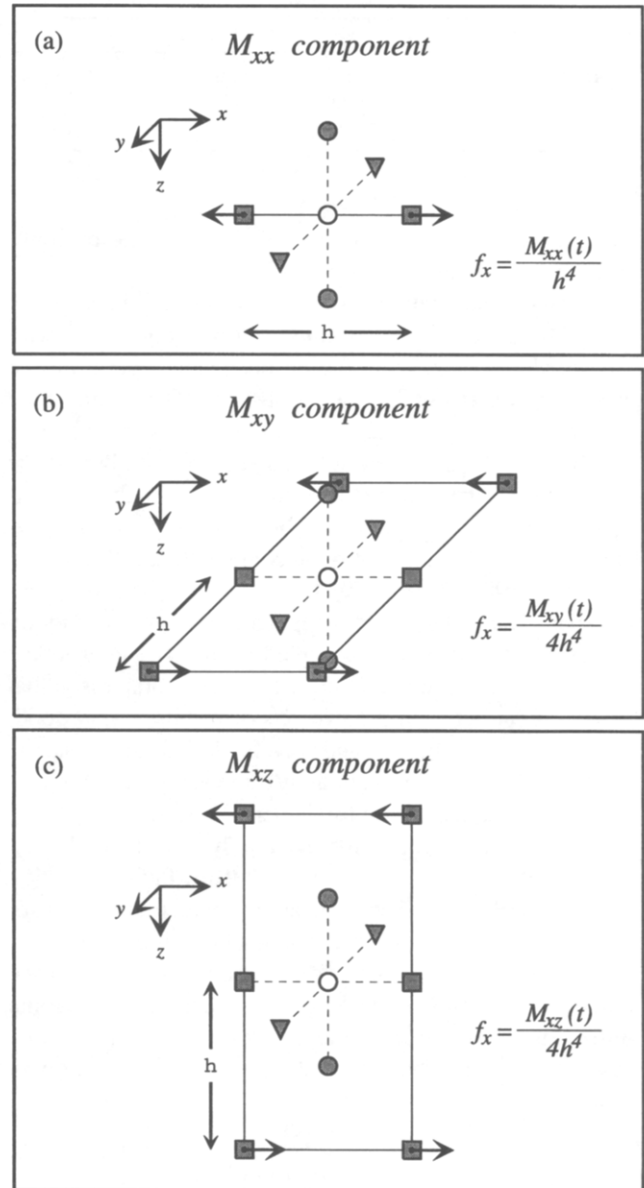


Figure 4. Representation of Cartesian moment-tensor components acting in the  $x$  direction using equivalent body-force components. For the  $f_x$  component, the forces are applied at the same location as the  $v_x$  component of the wave field. The symbols representing the wave-field variables in the above diagrams are the same as those defined in Figure 1. The strength of the body force applied at each point is given by the expression to the right of each diagram, and the force direction is indicated by the vectors shown in each of the diagrams. Similar representations can be made for the  $f_y$  and  $f_z$  force components.

Table 1  
Fundamental Fault Orientations

Fault Name	Fault Parameters			Observation Azimuth		
	Strike	Dip	Rake	Vertical	Radial	Tangential
DD	0°	45°	90°	45°	45°	no response
DS	90°	90°	90°	0°	0°	90°
SS	0°	90°	0°	45°	45°	0°

fundamental responses can be used to obtain the response for a fault of any arbitrary orientation.

For these calculations, we have used a half-space model ( $v_p = 4.0$  km/sec,  $v_s = 2.3$  km/sec,  $\rho = 1.8$  gm/cm<sup>3</sup>) with a source depth of 2.5 km and an observation point on the surface at a horizontal range of 10 km. The source time function is a triangle with a width of 1 sec. A grid spacing of 0.25 km and a time step of 0.025 sec were used in the FD computations. The time histories computed with the FD technique are compared with those obtained using a frequency-wavenumber (FK) integration technique (e.g., Wang and Herrmann, 1980; Saikia, 1994) in Figure 5. The FK technique has been widely used in applications of ground-motion synthesis and is generally accepted as an extremely robust and accurate technique. It is clear from this comparison that the agreement between the two sets of results is very good, both in terms of amplitude and waveform, indicating that the FD source formulation accurately represents the moment-tensor description of these fundamental faults.

Since the FD formulation accurately models the fundamental fault responses, it is inferred that any fault orientation can be modeled provided the appropriate moment-tensor components are used in expressions (11) through (13) and (B1). In addition, this source formulation can easily be used to model the response of heterogeneous rupture along a finite fault by distributing the moment-tensor point sources along an interface within the model chosen to represent the fault surface.

### Free-Surface Boundary

Free-surface boundary conditions often require careful consideration in finite-difference schemes because of concerns related to numerical stability and accuracy of the computed response (e.g., Alterman and Rotenberg, 1969; Ilan *et al.*, 1975; Bayliss *et al.*, 1986; Vidale and Clayton, 1986; Kosloff *et al.*, 1990; Zahradnik *et al.*, 1993). Here, we describe techniques for implementing a planar free-surface boundary for 3D problems utilizing fourth-order (or higher) spatial difference operators with the staggered-grid scheme.

### Zero-Stress Formulation

To represent a planar free-surface boundary in the staggered-grid scheme, an accurate and numerically stable formulation is easily implemented by explicitly satisfying the zero-stress condition at the free surface (e.g., Levander,

## Fundamental Fault Response

Half-space Model:  $h = 2.5$  km,  $r = 10$  km,  $M_0 = 10^{23}$  dyne-cm  
FD (solid) / FK (dashed)

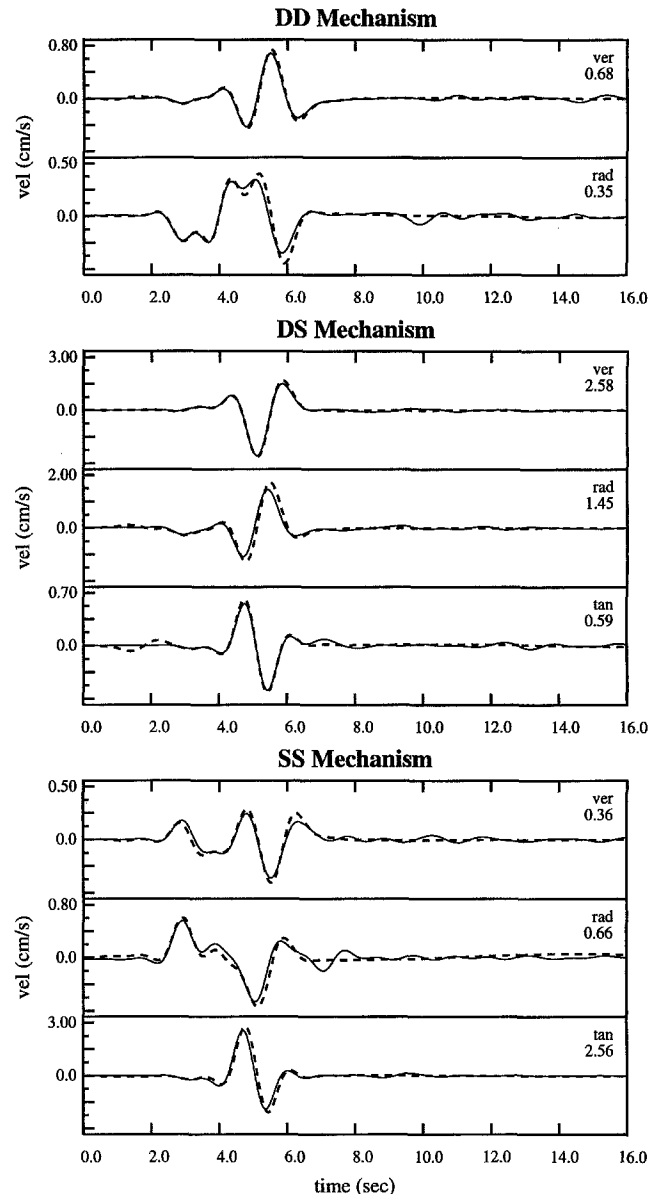


Figure 5. Comparison of seismograms calculated with the finite-difference (solid line) and the frequency-wavenumber (dashed line) techniques for the three fundamental fault orientations. The agreement between the results from the two techniques is very good, indicating the accuracy of the moment-tensor source formulation used in the finite-difference algorithm.

1988). Choosing the  $z$  axis as the vertical direction (positive downward) and setting the free surface at  $z = 0$ , we must satisfy the following expression:

$$\tau_{zz} = \tau_{xz} = \tau_{yz} = 0|_{z=0}. \quad (14)$$



Upon discretizing the model, particular values of the stress and velocity components need to be specified at and above the free-surface boundary in order to solve the interior system given by equations (5) and (6). Setting the free-surface boundary at  $iz = k$  (see Fig. 6), the values of the stress field at and above the free surface are obtained using the property of antisymmetry; i.e.,

$$\begin{aligned} \tau_{zz}: \tau_{zz}|_{iz=k} &= 0, & \tau_{zz}|_{iz=k-1} &= -\tau_{zz}|_{iz=k+1}; \\ \tau_{xz}: \tau_{xz}|_{iz=k-1/2} &= -\tau_{xz}|_{iz=k+1/2}, & \tau_{xz}|_{iz=k-3/2} &= -\tau_{xz}|_{iz=k+3/2}; \\ \tau_{yz}: \tau_{yz}|_{iz=k-1/2} &= -\tau_{yz}|_{iz=k+1/2}, & \tau_{yz}|_{iz=k-3/2} &= -\tau_{yz}|_{iz=k+3/2}. \end{aligned} \quad (15)$$

The variables  $\tau_{xx}$ ,  $\tau_{yy}$ , and  $\tau_{xy}$  are not needed above the boundary. Using these relations along with equations (2), we can derive the following difference equations for the velocity components at the free surface:

$$\begin{aligned} D_z v_z &= \frac{-\lambda}{(\lambda + 2\mu)} [D_x v_x + D_y v_y] |_{iz=k}, \\ D_z v_x &= -[D_z v_x + D_x v_z] |_{iz=k+1/2} - D_x v_z |_{iz=k-1/2}, \\ D_z v_y &= -[D_z v_y + D_y v_z] |_{iz=k+1/2} - D_y v_z |_{iz=k-1/2}. \end{aligned} \quad (16)$$

Given the interior values of  $v_x$ ,  $v_y$ , and  $v_z$  at and below the free surface (from equations 5), equations (16) can be solved using second-order difference operators (see Appendix A) to obtain the velocity components in the grid row just above the free surface.

To assess the accuracy of the zero-stress formulation in representing a planar free-surface boundary, we compare synthetic seismograms calculated using the staggered-grid FD technique with those obtained using the FK technique discussed earlier. Two models were analyzed: (1) a half-space model ( $v_p = 4.0$  km/sec,  $v_s = 2.3$  km/sec,  $\rho = 1.8$  gm/cm<sup>3</sup>) with an explosion source at a depth of 0.5 km and an observation point on the surface at a horizontal range of 20 km, and (2) a plane-layered model (M1), which is listed in Table 2 with a DD source (see Table 1) located at a depth of 2.6 km and an observation point on the surface at a distance of 10 km. The explosion and DD source mechanisms are particularly efficient in the excitation of Rayleigh waves at the free surface and thus provide a stringent test of the free-surface boundary formulation. In the FD calculations, model 1 has a time step of 0.025 sec and grid spacing of 0.25 km, and model 2 has a time step of 0.02 sec and grid spacing of 0.2 km. In order to focus on the free-surface response, we have not included the effects of anelastic attenuation in these calculations (i.e.,  $Q_p = Q_s = \infty$ ). For both models, a 1-sec triangle was used as the source time function, and the responses have been low-pass filtered at 1 Hz. At the upper frequency limit of 1 Hz, model 1 has over nine grid points per shear wavelength, and model 2 has five grid points per shear wavelength in the lowest-velocity region of the model.

Figure 7 displays the seismogram comparison for the two models. For the half-space model with the explosion

### Geometry of Free-Surface and Media Boundaries

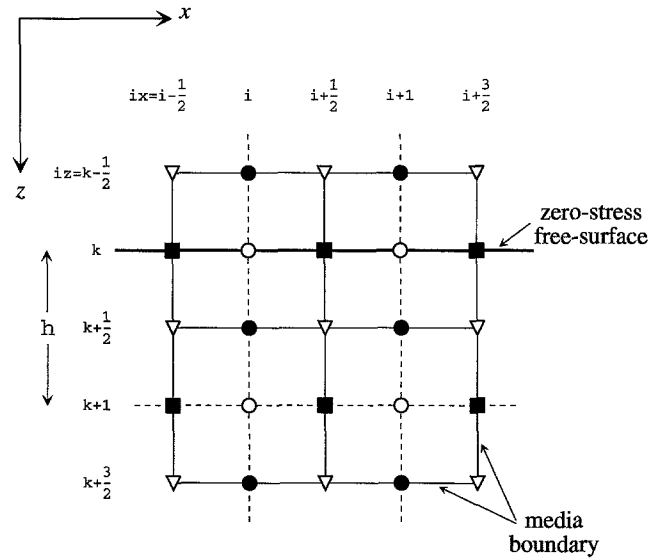


Figure 6. Layout of the field variables in an  $xz$  plane of the model space using the staggered-grid formulation. The media parameters  $\lambda$ ,  $\mu$ , and  $\rho$  are defined at the same locations as the normal stress components (open circles). For models with variable media, the boundaries between regions of different media are defined by the thin solid lines. The effective values of density and rigidity on these boundaries are determined using equations (8) and (9). The location of the zero-stress free-surface boundary is shown by the heavy solid line and is coincident with the location of the normal stress nodes.

Table 2  
Velocity Model M1

$v_p$ (km/sec)	$v_s$ (km/sec)	$\rho$ (g/cm <sup>3</sup> )	$th$ (km)
2.0	1.0	1.4	0.7
3.0	1.6	1.5	1.2
4.0	2.3	1.8	—

source, two distinct arrivals are apparent; the direct  $P$  wave at about 5 sec, and a very strong Rayleigh wave at about 9 sec. Clearly, the overall agreement between the responses obtained from the two computational techniques is very good for this model. In fact, the only noticeable difference is a slight underprediction in the amplitude of the Rayleigh wave on the radial component as computed by the FD method.

The lower panel of Figure 7 shows the comparison of results for the plane-layer model with DD source mechanism. In this case, the source radiates both  $P$  and  $S$  waves, and due to the layered velocity structure, a combination of direct, reflected, and converted phases, in addition to the surface waves, contributes to the computed ground-motion response.

However, despite the increased complexity of the model, the two techniques produce results that are in excellent agreement with one another.

In the above analysis, we have only considered models having a horizontal (planar) free-surface boundary. For this case, the zero-stress formulation provides a highly accurate, stable, and efficient method to model the response at the free surface. For the case of a dipping or irregular free-surface boundary, the zero-stress formulation becomes more difficult to formulate because the boundary is no longer naturally aligned with the layout of the FD grid. Techniques that locally rotate the grid coordinates (e.g., Jih *et al.*, 1988) or that deform the grid using a coordinate mapping (e.g., Tessmer *et al.*, 1992; Tessmer and Kosloff, 1994) have been successfully applied with the zero-stress formulation. However, these approaches can require a significant amount of numerical bookkeeping and may not be computationally practical for large 3D models.

#### Vacuum Formulation

An alternative method to model surface topography is to let  $v_p, v_s, \rho \rightarrow 0$  in the region above the free surface. This is the so-called vacuum formulation (e.g., Randall, 1989; Zahradnik *et al.*, 1993). This approach is attractive because it can be implemented with the same difference equations used in the interior of the model, and thus, the effects of surface topography are modeled in the same manner as internal media interfaces. However, numerical experiments show that this formulation is only stable for staggered-grid systems using second-order spatial difference operators, and unfortunately, for most 3D applications, second-order operators are inefficient because of the increased grid dimensions required to reduce numerical dispersion. Using fourth-order (or higher) spatial difference operators allows the use of a larger grid spacing, but these operators become unstable for regions where  $\rho \rightarrow 0$ .

In an attempt to stabilize the vacuum formulation for fourth-order systems, we have tried several variations of the above parameterization. In the one approach, which we refer to as the VF-O4 scheme, we allow  $v_p, v_s \rightarrow 0$ , while holding the density constant (or reducing only marginally) in the region above the free surface. In another approach, which we refer to as the VF-O24 scheme, we allow  $v_p, v_s, \rho \rightarrow 0$  above the free surface, but we apply second-order spatial difference operators locally at the free-surface boundary. A third approach, which we are currently testing, involves the use of more sophisticated formulations for the averaging of media parameters than those given by equations (8) and (9). Preliminary results indicate that stability can be achieved with this approach, however, the accuracy of the response is significantly degraded. Since this approach is still being investigated, we defer presentation of the details of this formulation to a later time.

Both the VF-O4 and VF-O24 schemes appear to yield stable calculations, yet they also suffer from numerical inaccuracies that limit their range of applicability. This is il-

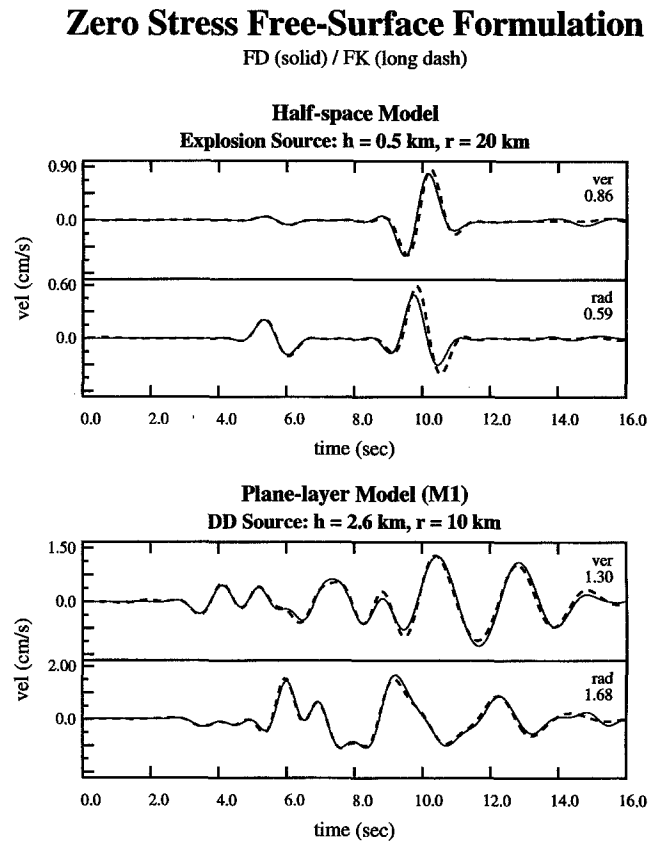


Figure 7. Comparison of seismograms calculated with the frequency-wavenumber technique (dashed line) and the finite-difference technique using the zero-stress free-surface formulation (solid line). The top panel shows the results for a half-space model, and the bottom panel shows the results for a plane-layered model. For both models, very good agreement is obtained between the results generated with each technique.

lustrated in Figure 8, which compares calculations obtained with these formulations against FK results computed for models similar to those discussed earlier in Figure 7. Because the free surface in the vacuum formulation lies along a media boundary that is one-half grid length ( $h/2$ ) from the depth level of the zero-stress boundary (see Fig. 6), we have increased the source depth by  $h/2$  for consistency in these comparisons. In addition, for the plane-layer structure, here we use a slight variation of model M1 (Table 2), which has a top layer with a thickness of 0.8 km instead of 0.7 km. We refer to this as model M2.

The VF-O4 scheme exhibits the most serious shortcomings, showing significant grid dispersion for Rayleigh-wave propagation along the free surface (Fig. 8). This scheme fails because the use of a nonzero value for the density above the free-surface boundary does not match the appropriate reflection coefficient for the vacuum formulation at the free surface (Zahradnik *et al.*, 1993). This allows energy propagating along the free surface to leak into the region above the

## Vacuum Free-Surface Formulation

VF-O24 (solid) / FK (long dash) / VF-O4 (short dash)

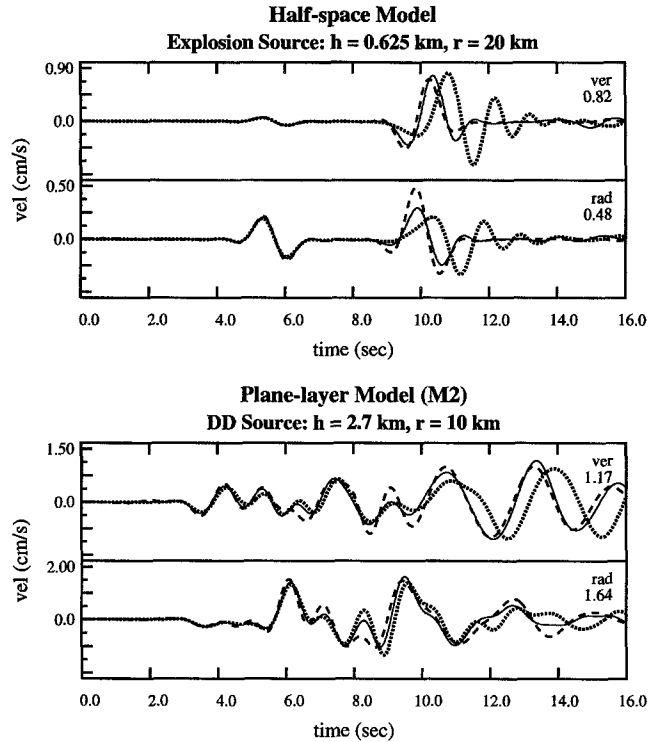


Figure 8. Comparison of seismograms calculated with the frequency-wavenumber technique (long-dashed line) and the finite-difference technique using the modified vacuum formulations for the free-surface boundary discussed in the text (VF-O4 and VF-O24). The VF-O4 formulation (short-dashed line) shows significant grid dispersion in the propagation of Rayleigh waves along the free surface. The VF-O24 formulation (solid line) does not appear to suffer any problems related to grid dispersion, but this approach does show some mismatch in the amplitude response of surface-reflected phases.

boundary, which has essentially zero-wave velocity. Since the energy is allowed to leak into this region, the Rayleigh wave senses the low velocities above the boundary and exhibits the characteristics of numerical grid dispersion. This phenomena is similar to the “ringing” described by Kosloff *et al.* (1990) when using a zero-velocity zone to model the free surface with the pseudospectral technique.

The VF-O24 scheme, on the other hand, does not appear to suffer any difficulties related to grid dispersion at the free-surface boundary. However, the amplitudes of the surface waves and surface-reflected phases generated by this formulation are not as accurate as those obtained by the zero-stress formulation shown in Figure 7. This probably results from a slight mismatch in the reflection coefficient obtained at the free surface with the VF-O24 scheme due to the transition from fourth-order to second-order difference operators near the free-surface boundary.

Of the two approaches considered here (i.e., the VF-O4 and VF-O24 schemes), the VF-O4 scheme suffers noticeably from the effects of numerical grid dispersion for surface-wave propagation along the free-surface boundary, and therefore, the VF-O24 scheme currently appears to be the better approach for modeling the free-surface boundary using the vacuum formulation. However, since we have not analyzed the performance of the VF-O24 scheme for the case of a nonplanar free-surface boundary, the stability and accuracy of this approach to model surface topography still need to be investigated.

## Modeling Anelastic Attenuation

Incorporating viscoelasticity within time-stepping wave-field simulations is difficult because a straightforward application of such models in the time domain requires a convolutional relation between stress and strain. Algorithms that replace the convolutional operators with a system of relaxation functions circumvent this problem, but at a substantial increase in storage and computation time (e.g., Day and Minster, 1984; Emmerich and Korn, 1987; Carcione *et al.*, 1988). Here, we describe an approximate technique for modeling spatially varying viscoelastic media within finite-difference calculations using a simple time domain attenuation operator. The implementation of this operator is not restricted to staggered-grid formulations and can be generally applied to any discrete-grid time domain technique. In addition, although we follow a different derivation approach, the attenuation operator we present is similar in form to that originally described by Zahradnik *et al.* (1990a, 1990b) for the special case of SH waves with spatially constant attenuation.

In the frequency domain, anelastic attenuation operators are well understood and easy to implement using the parameter  $Q$ , which is the quality factor of the medium (Aki and Richards, 1980, p. 168). In the limit  $Q \rightarrow \infty$ , the medium is purely elastic; for finite values of  $Q$ , the medium behaves in a viscoelastic manner. Assuming  $Q$  is independent of frequency, anelasticity can be modeled by allowing the elastic wave speed  $c_e$  to take the form

$$c_e \rightarrow c_1 \left[ 1 + \frac{1}{\pi Q} \ln \left( \frac{\omega}{2\pi} \right) - \frac{i}{2Q} \right], \quad (17)$$

where  $c_1$  is the body-wave phase velocity at a reference frequency of 1 Hz (Aki and Richards, 1980, p. 182). If we consider a plane wave traveling in a homogeneous medium, this will give a propagation term of the form

$$P = \exp[i\omega(r/c_w - t)] \quad (18)$$

and an attenuation term of the form

$$A = \exp \left[ \frac{-\omega r}{2c_1 Q} \right], \quad (19)$$

which is correct to first order in  $Q$ . Here,  $r$  is the distance of propagation, and  $c_w$ , the frequency-dependent phase velocity, is given by

$$c_w = c_1 \left[ 1 + \frac{1}{\pi Q} \ln \left( \frac{\omega}{2\pi} \right) \right], \quad (20)$$

where the frequency dispersion is necessary to ensure causality.

For broadband analyses, the correct form of the frequency dependence in equations (19) and (20) is required to produce accurate results. However, for limited bandwidth analyses, these equations can be approximated by using an appropriate reference frequency. This simplifies the expressions by removing the explicit dependence on frequency. In addition, since the variations in phase velocity are typically less than 1 to 2% for the period range 1 to 20 sec, the reference value  $c_1$  can be used as a good approximation to  $c_w$  in this bandwidth.

For the attenuation term, choosing a reference frequency of  $\omega = 2\pi f_0$  gives us

$$A = \exp \left[ \frac{-\pi f_0 t}{Q} \right], \quad (21)$$

where we have set  $t = r/c_1$  as the travel time. Equation (21) implies that  $Q$  is no longer independent of frequency, but has the linear form

$$Q = Q_0 \frac{f}{f_0}, \quad (22)$$

where  $Q_0$  is the frequency-independent quality factor. When  $f$  is near the reference frequency  $f_0$ , the approximation to constant  $Q$  works very well. A good rule of thumb is to choose the reference frequency  $f_0$  to be near the peak frequency of the source and to specify a simulation bandwidth that is centered around this value. Relative to the constant  $Q$  model, energy for frequencies greater than  $f_0$  will be underattenuated, and energy for frequencies less than  $f_0$  will be overattenuated.

In the preceding analysis, we have only considered one wave speed ( $c_1$ ) and one value of  $Q$ . In theory, we should distinguish between  $P$  and  $S$  waves and apply the appropriate attenuation operator ( $Q_p$  or  $Q_s$ ) to the particular wave field. In practice, this is difficult because the finite-difference calculation does not explicitly separate  $P$  and  $S$  energy. Calculating the divergence and curl of the wave field at each time step to determine the  $P$  and  $S$  energy partitions is possible but can be cumbersome and time-consuming. In light of the approximations that we have employed in deriving the attenuation term (equation 21) and since earthquake motions

are typically dominated by shear-wave (or surface-wave) energy, it is probably adequate to use a  $Q$  function that is appropriate for shear waves. This means that, in general,  $P$  waves will be overattenuated, since  $Q_p$  is usually larger than  $Q_s$ .

Implementation of the attenuation term given by equation (21) within the finite-difference calculations is a trivial matter. Using sequential applications of equations (5) and (6), the velocity and stress fields are propagated from one time step to the next. Attenuation is accommodated at each time step by multiplying the updated velocity field determined from equations (5) and the updated stress field determined from equations (6) with the attenuation function given by

$$A(x, y, z) = \exp \left[ \frac{-\pi f_0 \Delta t}{Q_s(x, y, z)} \right], \quad (23)$$

where  $Q_s(x, y, z)$  is the media-dependent (spatially variable)  $Q$  function for shear waves. The reason that the attenuation function must be applied to both the updated velocity field and the updated stress field is because both fields are propagated during each time update.

In a strict sense, the attenuation function given by equation (23) is only valid for plane waves propagating in a homogeneous medium. However, in allowing  $Q$  to be spatially variable, we have relaxed this restriction by assuming that the media is homogeneous in the immediate vicinity of each grid point. Within locally homogeneous regions of large-scale heterogeneous media, this assumption is clearly valid. In regions near media interfaces where  $Q$  changes, this assumption can also be justified because the numerical stability condition (equation A6) requires  $\Delta t$  to be sufficiently small so that the wave energy can only propagate a fraction of a grid step at each time update. Therefore, the wave field travels only a short distance relative to the size of the grid spacing at each time update, and it takes several time updates (at a minimum) for wave energy to travel from one grid point to the next. Since the transmission of energy across an interface located between adjacent grid points represents the integrated effect of a number of time updates, then for each individual time step, the wave field is most sensitive to the (locally homogeneous) attenuation function defined at each specific grid point.

In order to test the accuracy of the attenuation operator used in the FD technique, we compare FD simulation results with those obtained by the FK technique for three cases: (1) an infinite  $Q$  model, (2) a spatially variable  $Q$  model, and (3) a spatially constant  $Q$  model. For these calculations, we use the plane-layered velocity structure (M1) listed in Table 2 with an SS source at a depth of 1.6 km and an observation point on the surface at a horizontal range of 10 km. For the spatially variable  $Q$  model, the top layer has  $Q_p = 20$  and  $Q_s = 10$ , with  $Q = \infty$  for all other layers. The spatially constant  $Q$  model is designed as an approximation for the

spatially variable  $Q$  model, and in this case,  $Q$  is set to 10 for all layers in the model. For this example, we have chosen rather low  $Q$  values in order to highlight the effects of anelasticity on the various phases. The source time function is a 1-sec triangle, and the results have been low-pass filtered at 1 Hz. A reference frequency of 0.5 Hz ( $T = 2$  sec) was used for the  $Q$  operator in the FD calculation. Figure 9 compares the simulated time histories.

Many aspects of source and wave propagation phenomena are illustrated in this simple example, including the effects of source radiation pattern, free surface interactions, conversions between  $P$  and  $S$  energy, reflection and transmission at media interfaces, and surface-wave development. In addition, by comparing both spatially constant and spatially variable  $Q$  formulations, we can examine the validity of using the media-dependent attenuation operator in the FD calculation.

Overall, the seismograms in Figure 9 show very good agreement between the FD and FK results for both the infinite  $Q$  and the two finite  $Q$  models. Due to the use of a relatively low  $Q$  value, the results for the spatially constant  $Q$  model show a significant reduction in amplitude relative to the results of the infinite  $Q$  model. Yet even with a large amount of attenuation, the FD formulation matches the FK result very well. In the spatially variable  $Q$  model, the amount of attenuation experienced by a given phase depends on its particular propagation path. For example, surface waves are attenuated much more than body waves because they are trapped in the upper (low  $Q$ ) layers of the model. The favorable comparison demonstrated in Figure 9 for the spatial variable  $Q$  model indicates that these effects are modeled very nicely using the media-dependent  $Q$  operator in the FD calculation. This result supports the validity of using the spatially variable form of the attenuation operator in FD calculations and demonstrates the effectiveness of this formulation when the attenuation parameters are media dependent.

As mentioned earlier, the attenuation model used in the FD calculations will underattenuate energy at frequencies higher than the reference frequency  $f_0$  and will overattenuate energy at frequencies less than  $f_0$ . Since the triangular source pulse is peaked around a 1-sec period and the reference frequency for the attenuation term in the FD calculation was chosen at 0.5 Hz ( $T = 2$  sec), the agreement for the body-wave phases between the two techniques is excellent. At longer periods, the FD results show somewhat more damping than the FK results, as indicated by the slight over-attenuation of surface waves in the FD calculation compared to the FK seismograms. However, since the absolute energy levels in the longer-period bandwidth is relatively small, the overall effect of this mismatch is not very significant.

## Discussion and Conclusions

The flexibility and accuracy of the staggered-grid finite-difference algorithm make this technique a powerful tool in the analysis of wave propagation problems. This article out-

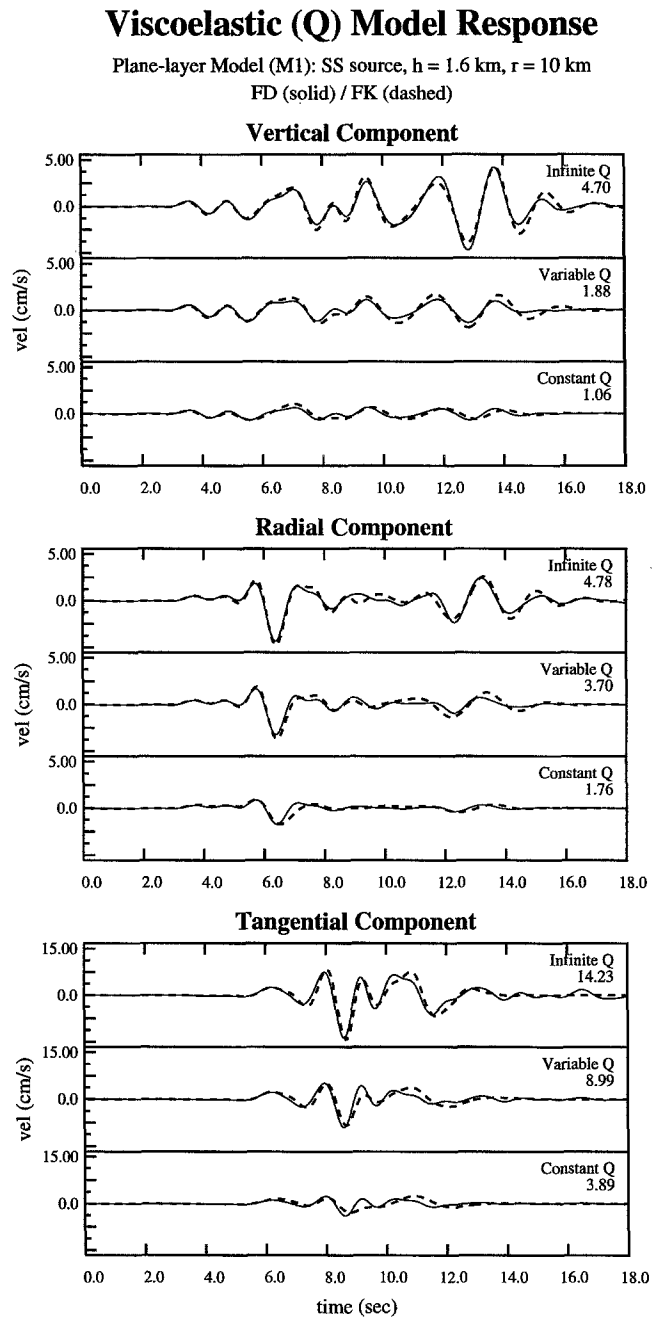


Figure 9. Comparison of seismograms calculated with the finite-difference (solid line) and frequency-wavenumber (dashed line) techniques for models with infinite, spatially variable, and spatially constant values of  $Q$ . For each component, the top pair of traces shows the infinite  $Q$  model results (labeled Infinite  $Q$ ), the middle pair of traces shows the spatially variable  $Q$  model results (labeled Variable  $Q$ ), and the bottom pair of traces shows the spatial constant  $Q$  model results (labeled Constant  $Q$ ). In all cases, the agreement between the results from the two techniques is very good, even when rather low values of  $Q$  are used.

lines the basic formulation of a 3D elastic wave-field simulation algorithm based on the staggered-grid finite-difference approach. In order to keep the scope of this presentation at a general level, we have omitted a detailed discussion of issues related to the development of higher-order absorbing boundary conditions, stability analysis of the discrete system, and numerical grid dispersion. The articles by Virieux (1986), Levander (1988), and Randall (1989) provide more complete analyses of these issues.

In addition to presenting a general outline of the staggered-grid approach for 3D elastic problems, this article also discusses issues related to the incorporation of realistic representations of seismic sources and geologic media within the finite-difference calculations. Specifically, the issues addressed here are (1) the implementation of a moment-tensor source formulation for the staggered-grid system, (2) modeling a planar free-surface boundary response in a stable and appropriate manner, and (3) the development of an approximate technique for modeling spatially varying viscoelastic media with time domain attenuation operators. The examples and comparisons shown in this article demonstrate that the staggered-grid formulation provides a highly accurate and efficient method for the simulation of elastic wave propagation in 3D media. Furthermore, although not specifically addressed here, one of the primary advantages of the staggered-grid system is its ability to model complicated, heterogeneous media in a straightforward and stable manner (e.g., Levander, 1988; Randall *et al.*, 1991; Yomogida and Etgen, 1993; Olsen *et al.*, 1995).

While the finite-difference simulation of 3D elastic wave fields in large-scale geologic models can be computationally demanding, it does not represent an unreachable goal. By utilizing the memory optimization procedure described in this article, large-scale 3D finite-difference simulations can be computed in a routine manner using only a single-processor desktop workstation. This fact is illustrated by the data in Table 3, which summarizes the model parameters and CPU run times for recent 3D elastic finite-difference simulations of the 1987 Whittier Narrows earthquake (Graves, 1996b) and the 1995 Kobe, Japan, earthquake (Graves, 1996a). These simulations were run on a workstation platform that consists of a Sun Sparcstation with a single 125-MHz processor, 192 Mbytes of core memory, and a 2-Gbyte hard disk.

To date, the simulation of the 1995 Kobe earthquake is the largest computation that we have conducted using the workstation approach. The model consists of  $1.44 \times 10^7$  grid points and required 104 sec of CPU to perform each time update, for a total of 175 CPU hours to produce 90 sec (6000 time steps) of simulated motions. To put these numbers into perspective, we compare our run time parameters for the Kobe simulation with those reported by Olsen *et al.* (1995) for their 3D finite-difference simulation of a hypothetical event on the San Andreas fault in Southern California. The Olsen *et al.* model is slightly larger than the Kobe

Table 3  
Model Parameters and CPU Times for 3D Finite-Difference Workstation Simulations

	Whittier Narrows	Kobe
Model dimensions ( $nx \times ny \times nz$ )	$250 \times 250 \times 90$	$400 \times 300 \times 120$
Total time steps	3000	6000
Grid spacing (km)	0.2	0.2
Time step (sec)	0.01	0.015
Minimum velocity (km/sec)	1.0	0.55
Maximum frequency resolution (Hz)*	1.0	0.5
Model size (total grid points)	$5.625 \times 10^6$	$1.44 \times 10^7$
CPU per time step (sec)	40	104
Total CPU (hours)	33	175

\*The maximum frequency resolution is the highest frequency that can be modeled with a sampling of at least 5 grid points per wavelength in the lowest-velocity region of the model.

model ( $2.35 \times 10^7$  versus  $1.44 \times 10^7$  grid points) and required a computation time of 17 sec per time update using a supercomputer with 512 parallel processors. Normalizing by the difference in model size between these two simulations and the number of processors used in each calculation, the workstation-based approach described here is effectively 30 times more efficient per processor than the supercomputer approach. Obviously, due to the large number of processors, the supercomputer simulation requires less total computation time than the workstation simulation (about a factor of 10). However, even with the increased run time, the workstation approach is far more practical because the computational hardware is relatively inexpensive (compared to a supercomputer), and these platforms are already widely available.

Utilizing the workstation simulation technique described in this article, we have an efficient and practical research tool that can be used to compute the expected nature of long-period ground motions for earthquakes occurring in areas containing complex geology. This 3D simulation technique has been successfully applied to the Marina District of San Francisco (Graves, 1993), the Portland and Puget Sound regions of the U.S. Pacific Northwest (Graves, 1994a and 1994b), the Los Angeles region of southern California (Graves, 1995, 1996b), and the Osaka region in Japan (Graves, 1996a). The results of these studies provide quantitative estimates of the effects of 3D geology on long-period strong ground motions generated during large earthquakes.

### Acknowledgments

The ideas leading to the formulation of the memory optimization procedure were developed during a series of discussions with Robert Clayton. Other discussions with Curtis Randall and Alan Levander helped to formulate and clarify some of the ideas presented in this article. The reviews provided by Peter Moczo and Jean Virieux were extremely helpful and led to significant improvements in the quality of the manuscript. This research

was sponsored in part by USGS Grant Numbers 1434-93-G-2327 and 1434-94-G-2433.

## References

- Aki, K. and P. G. Richards (1980). *Quantitative Seismology*, W. H. Freeman and Co., San Francisco.
- Alterman, Z. and A. Rotenberg (1969). Seismic waves in a quarter plane, *Bull. Seism. Soc. Am.* **59**, 347–368.
- Bayliss, A., K. E. Jordan, B. J. LeMesurier, and E. Turkel (1986). A fourth-order accurate finite-difference scheme for the computation of elastic waves, *Bull. Seism. Soc. Am.* **76**, 1115–1132.
- Boore, D. M. (1972). Finite-difference methods for seismic wave propagation in heterogeneous materials, in *Methods in Computational Physics*, Vol. 11, B. A. Bolt (Editor), Academic Press, New York.
- Carcione, J. M., D. Kosloff, and R. Kosloff (1988). Wave propagation simulation in a linear viscoelastic medium, *Geophys. J. Int.* **95**, 597–611.
- Clayton, R. W. and B. Engquist (1977). Absorbing boundary conditions for acoustic and elastic wave equations, *Bull. Seism. Soc. Am.* **67**, 1529–1540.
- Coutant, O., J. Virieux, and A. Zollo (1995). Numerical source implementation in a 2D finite difference scheme for wave propagation, *Bull. Seism. Soc. Am.* **85**, 1507–1512.
- Day, S. M. and J. B. Minster (1984). Numerical simulation of wave fields using a Padé approximant method, *Geophys. J. Int.* **78**, 105–118.
- Emmerich, H. and M. Korn (1987). Incorporation of attenuation into time-domain computations of seismic wave fields, *Geophysics* **52**, 1252–1264.
- Frankel, A. (1993). Three-dimensional simulations of ground motions in the San Bernardino Valley, California, for hypothetical earthquakes on the San Andreas fault, *Bull. Seism. Soc. Am.* **83**, 1020–1041.
- Graves, R. W. (1993). Modeling three-dimensional site response effects in the Marina District basin, San Francisco, California, *Bull. Seism. Soc. Am.* **83**, 1042–1063.
- Graves, R. W. (1994a). Rupture history and strong ground motion modeling of the 1992 Cape Mendocino earthquake, *Seism. Res. Lett.* **65**, 40.
- Graves, R. W. (1994b). Modeling the long period (1–20 sec) basin response in the Puget Sound region for hypothetical Cascadia subduction zone earthquakes, *EOS* **75**, 441.
- Graves, R. W. (1995). Preliminary analysis of long period basin response in the Los Angeles region from the 1994 Northridge earthquake, *Geophys. Res. Lett.* **22**, 101–104.
- Graves, R. W. (1996a). Simulating realistic earthquake ground motions in regions of deep sedimentary basins, *Proc. of the 11th World Conference on Earthquake Engineering*, Acapulco, Mexico, 23–28 June 1996.
- Graves, R. W. (1996b). 3D elastic finite-difference modeling of the 1987 Whittier Narrows earthquake, manuscript in preparation.
- Herrmann, R. B. and C. Y. Wang (1985). A comparison of synthetic seismograms, *Bull. Seism. Soc. Am.* **75**, 41–56.
- Ilan, A., A. U. Ungar, and Z. Alterman (1975). An improved representation of boundary conditions in finite-difference schemes for seismological problems, *Geophys. J. R. Astr. Soc.* **43**, 727–745.
- Jih, R. S., K. L. McLaughlin, and Z. A. Der (1988). Free-boundary conditions of arbitrary topography in a two-dimensional explicit elastic finite-difference scheme, *Geophysics* **53**, 1045–1055.
- Kosloff, D., D. Kessler, A. Q. Filho, E. Tessmer, A. Behle, and R. Strahlitz (1990). Solution of the equations of dynamic elasticity by a Chebyshev spectral method, *Geophysics* **55**, 734–748.
- Kummer, B., A. Behle, and F. Dorau (1987). Hybrid modeling of elastic-wave propagation in two-dimensional laterally inhomogeneous media, *Geophysics* **52**, 765–771.
- Levander, A. R. (1988). Fourth-order finite-difference P-SV seismograms, *Geophysics* **53**, 1425–1436.
- Madariaga, R. (1976). Dynamics of an expanding circular fault, *Bull. Seism. Soc. Am.* **66**, 163–182.
- Moczo, P. (1989). Finite-difference technique for SH-waves in 2-D media using irregular grids-application to the seismic response problem, *Geophys. J. Int.* **99**, 321–329.
- Olsen, K. B., R. J. Archuleta, and J. R. Matarese (1995). Magnitude 7.75 earthquake on the San Andreas fault: three-dimensional ground motion in Los Angeles, *Science* **270**, 1628–1632.
- Randall, C. J. (1989). Absorbing boundary condition for the elastic wave equation: velocity-stress formulation, *Geophysics* **54**, 1141–1152.
- Randall, C. J., D. J. Scheibner, and P. T. Wu (1991). Multiple borehole acoustic waveforms: synthetic logs with beds and borehole washouts, *Geophysics* **56**, 1757–1769.
- Saikia, C. K. (1994). Modified frequency-wavenumber algorithm for regional seismograms using Filon's quadrature: modelling of  $L_g$  waves in eastern North America, *Geophys. J. Int.* **118**, 142–158.
- Tessmer, E. and D. Kosloff (1994). 3-D elastic modeling with surface topography by a Chebyshev spectral method, *Geophysics* **59**, 464–473.
- Tessmer, E., D. Kosloff, and A. Behle (1992). Elastic wave propagation simulation in the presence of surface topography, *Geophys. J. Int.* **108**, 621–632.
- Vidale, J. E. and R. W. Clayton (1986). A stable free-surface boundary condition for two-dimensional elastic finite-difference wave simulation, *Geophysics* **51**, 2247–2249.
- Virieux, J. (1984). SH wave propagation in heterogeneous media: velocity-stress finite-difference method, *Geophysics* **49**, 1933–1957.
- Virieux, J. (1986). P-SV wave propagation in heterogeneous media: velocity-stress finite-difference method, *Geophysics* **51**, 889–901.
- Wang, C. Y. and R. B. Herrmann (1980). A numerical study of P-, SV-, and SH-wave generation in a plane layered medium, *Bull. Seism. Soc. Am.* **70**, 1015–1036.
- Yomogida, K. and J. T. Etgen (1993). 3-D wave propagation in the Los Angeles Basin for the Whittier-Narrows earthquake, *Bull. Seism. Soc. Am.* **83**, 1325–1344.
- Zahradník, J., J. Jech, and P. Moczo (1990a). Approximate absorption corrections for complete SH seismograms, *Studia Geoph. Geod.* **34**, 185–196.
- Zahradník, J., J. Jech, and P. Moczo (1990b). Absorption correction for computations of a seismic ground response, *Bull. Seism. Soc. Am.* **80**, 1382–1387.
- Zahradník, J., P. Moczo, and F. Hron (1993). Testing four elastic finite-difference schemes for behavior at discontinuities, *Bull. Seism. Soc. Am.* **83**, 107–129.

## Appendix A

### Staggered-Grid Finite-Difference Operators

Here, we present second-order and fourth-order spatial difference operators for use in equations (5) and (6). Coefficients for these and higher-order operators are easily determined using the technique described by Yomogida and Etgen (1993).

The spatial derivatives in equations (5) and (6) are given by expressions of the form

$$\frac{\partial}{\partial x} v_x \approx D_x v_x |_{i,j,k}, \quad (\text{A1})$$

where  $D_x$  represents the discrete form of the differential operator  $\partial/\partial x$  acting on the variable  $v_x$ , and evaluated at the point  $x = i\Delta x$ ,  $y = j\Delta y$ ,  $z = k\Delta z$ . With a uniform grid

spacing of  $h$  (i.e.,  $\Delta x = \Delta y = \Delta z = h$ ), the second-order  $O(h^2)$  form of this operator is

$$D_x v_x|_{i,j,k} = \frac{1}{h} [v_{xi+1/2,j,k} - v_{xi-1/2,j,k}] \quad (\text{A2})$$

(Virieux, 1986), and the fourth-order  $O(h^4)$  form is

$$D_x v_x|_{i,j,k} = \frac{1}{h} \{ c_0 [v_{xi+1/2,j,k} - v_{xi-1/2,j,k}] - c_1 [v_{xi+3/2,j,k} - v_{xi-3/2,j,k}] \}, \quad (\text{A3})$$

where  $c_0 = 9/8$  and  $c_1 = 1/24$  (Levander, 1988). The stability criterion for the 3D system is given by

$$\Delta t < \frac{h}{v_{\max} \sqrt{3}} \left[ \sum_{m=0}^N c_m \right]^{-1}, \quad (\text{A4})$$

where  $v_{\max}$  is the maximum wave speed and  $c_m$  are the coefficients of the difference operator. For the second-order system,  $N = 0$  and  $c_0 = 1$ , and we obtain the relation

$$\Delta t < \frac{h}{v_{\max} \sqrt{3}}. \quad (\text{A5})$$

And similarly, for the fourth-order system, we obtain

$$\Delta t < 0.495 \frac{h}{v_{\max}}. \quad (\text{A6})$$

In addition, the second-order system requires a minimum sampling of 10 grid points/wavelength (Virieux, 1986), and the fourth-order system requires a minimum sampling of 5 grid points/wavelength (Levander, 1988).

## Appendix B

### $f_y$ and $f_z$ Body-Force Components of the Moment-Tensor Source

Expressions for the distributions of body-force components  $f_y$  and  $f_z$  due to a moment-tensor source can be de-

rived in a similar manner as that discussed in the text for the  $f_x$  component. For a source centered at the grid location  $x = ih$ ,  $y = jh$ ,  $z = kh$ , these expressions are

$$\begin{aligned} f_{yi,j+1/2,k} &= \frac{M_{yy}(t)}{h^4} & f_{zi,j,k+1/2} &= \frac{M_{zz}(t)}{h^4} \\ f_{yi,j-1/2,k} &= \frac{-M_{yy}(t)}{h^4} & f_{zi,j,k-1/2} &= \frac{-M_{zz}(t)}{h^4} \\ f_{yi+1,j-1/2,k} &= \frac{M_{xy}(t)}{4h^4} & f_{zi+1,j,k-1/2} &= \frac{M_{xz}(t)}{4h^4} \\ f_{yi+1,j+1/2,k} &= \frac{M_{xy}(t)}{4h^4} & f_{zi+1,j,k+1/2} &= \frac{M_{xz}(t)}{4h^4} \\ f_{yi-1,j-1/2,k} &= \frac{-M_{xy}(t)}{4h^4} & f_{zi-1,j,k-1/2} &= \frac{-M_{xz}(t)}{4h^4} \\ f_{yi-1,j+1/2,k} &= \frac{-M_{xy}(t)}{4h^4} & f_{zi-1,j,k+1/2} &= \frac{-M_{xz}(t)}{4h^4} \\ f_{yi,j-1/2,k+1} &= \frac{M_{yz}(t)}{4h^4} & f_{zi,j+1,k-1/2} &= \frac{M_{yz}(t)}{4h^4} \\ f_{yi,j+1/2,k+1} &= \frac{M_{yz}(t)}{4h^4} & f_{zi,j+1,k+1/2} &= \frac{M_{yz}(t)}{4h^4} \\ f_{yi,j-1/2,k-1} &= \frac{M_{yz}(t)}{4h^4} & f_{zi,j-1,k-1/2} &= \frac{M_{yz}(t)}{4h^4} \\ f_{yi,j+1/2,k-1} &= \frac{-M_{yz}(t)}{4h^4} & f_{zi,j-1,k+1/2} &= \frac{-M_{yz}(t)}{4h^4}. \end{aligned} \quad (\text{B1})$$

Woodward-Clyde Federal Services  
566 El Dorado Street  
Pasadena, California 91101

Manuscript received 15 November 1995.